



# Highly durable and active $\text{Co}_3\text{O}_4$ nanocrystals supported on carbon nanotubes as bifunctional electrocatalysts in alkaline media

Shuai Zhao <sup>a,b</sup>, Brian Rasimick <sup>a</sup>, William Mustain <sup>b</sup>, Hui Xu <sup>a,\*</sup>

<sup>a</sup> Giner, Inc., Newton, MA 02466, United States

<sup>b</sup> Department of Chemical & Biomolecular Engineering, University of Connecticut, Storrs, CT 06269, United States

## ARTICLE INFO

### Article history:

Received 28 May 2016

Received in revised form 29 August 2016

Accepted 23 September 2016

Available online 24 September 2016

### Keywords:

Oxygen reduction reaction

Oxygen evolution reaction

Alkaline media

Hybrid structure

Carbon nanotube

## ABSTRACT

Unitized regenerative alkaline membrane fuel cells (AMFCs) have recently attracted great attention as both an energy conversion and energy storage technology due to their low cost and high-energy storage density for renewable resources. The oxygen electrode has long been one of the primary limiting factors of reversible AMFCs due to the sluggish kinetics of the oxygen reduction and evolution reactions (ORR and OER, respectively). It is challenging to develop durable and efficient bifunctional ORR/OER electrocatalysts; in particular, few researchers have focused on the durability of the material, which is the most relevant aspect for industrial application of these catalysts. In this work, we present an optimized procedure producing a highly stable bifunctional hybrid catalyst with excellent ORR/OER activities. This catalyst comprises covalently-bonded hybrid structures of cobalt oxide nanocrystals decorated on pre-oxidized carbon nanotubes. We performed the durability test in a broad potential range, from 0.0 V to 1.9 V (vs. RHE), which is a harsh condition under which to our knowledge no previous hybrid structure in literature has survived. We have also linked the catalyst durability to metal oxide anchoring sites and its synthesis parameters. This study provides novel perspectives for the design of carbon-based, hybrid materials and insight into the synthesis–property relationships for the next-generation electrocatalysts.

© 2016 Elsevier B.V. All rights reserved.

## 1. Introduction

The unitized regenerative fuel cell, which at its core is an integration of fuel cell and electrolyzer in the same stack, has received significant attention as an alternative technology for energy conversion and storage. Among these unitized reversible fuel cells, reversible alkaline membrane fuel cells (AMFCs) have become increasingly attractive over the past few years due to their potential low cost and high energy storage capacity. Unfortunately, the adoption of reversible AMFCs has been challenging due to limited membrane stability and poor electrode reaction kinetics [1,2]. Therefore, developing high-performance oxygen reduction reaction (ORR)/oxygen evolution reaction (OER) bifunctional catalysts is considered one of the most critical needs to enable the commercial viability of reversible AMFCs.

Modified transition metal oxides [3–7] and novel synthesis techniques [8] have been shown to lead to catalysts with improved ORR/OER activities and durability, but they still generally suffer from poor dispersion and low conductivity with slow charge car-

rier mobility. Carbon nanotubes (CNTs) have been extensively used as electrode materials in many energy storage systems because of their high electronic conductivity and excellent stability [9–13]. Therefore, hybrid transition metal oxide–CNT structures have become popular in recent bifunctional catalyst studies [14–18]. Dai et al. discovered excellent ORR activity for  $\text{Co}_3\text{O}_4$  supported on reduced graphene oxide, which also showed reasonable OER activity [19]. Liang et al. found that the ORR activity can even be enhanced by incorporating Mn into the  $\text{Co}_3\text{O}_4$  lattice to increase the catalytic sites in the same hybrid structure using the same synthesis technique [20]. Later, Singh et al. proposed an approach to synthesize  $\text{Co}_3\text{O}_4$  supported on N-doped graphene with preferential exposure of low surface energy facets, which showed a low overpotential ( $\sim 280$  mV) for OER at a current density of  $10 \text{ mA cm}^{-2}$  [21]. S. Mao et al. reported high-performance ORR/OER bifunctional 3D crumpled graphene–cobalt oxide nanohybrids, which were amongst the best-performing non-PGM OER catalysts in 2014 [22]. Though catalysts with high activity have been shown, almost none of these studies discussed the durability of these bifunctional catalysts in the combined potential range of both ORR and OER reactions.

In the present work, we report a procedure to develop durable and active bifunctional ORR/OER electrocatalysts in alkaline media.

\* Corresponding author.

E-mail addresses: [hxu@ginerinc.com](mailto:hxu@ginerinc.com), [huixshu@gmail.com](mailto:huixshu@gmail.com) (H. Xu).

We synthesized catalysts with hybrid structures (metal oxides on functionalized CNTs) that can survive the harsh ORR/OER environments (from 0.0 V to 1.9 V) and demonstrate long-term stability for the first time. We also identified rational durability-mechanism-synthesis relationship for the application of hybrid electrocatalysts for reversible AMFCs. The hybrid structure was achieved by nucleating cobalt oxides on functionalized CNTs through hydrolysis and hydrothermal treatment. The supported catalyst was subsequently reduced to repair the CNTs as much as possible to minimize the number of corrosion sites. A combination of physical and electrochemical characterization techniques were used to analyze the effect of synthesis parameters upon catalyst durability and activity.

## 2. Experimental section

### 2.1. Pre-oxidation of CNTs

Potassium permanganate and nitric acid were compared as oxidation agents to understand the metal oxide growth mechanism. Two batches of 0.2 g commercial CNTs doped with nitrogen (3–5 wt%, 20–50 nm in outer diameter, US Research Nanomaterials, Inc.) were oxidized with a mixture of  $\text{KMnO}_4$  (Sigma-Aldrich, 1:1 weight ratio to CNTs) and 20 mL concentrated  $\text{H}_2\text{SO}_4$  (98%, Sigma-Aldrich) stirring at room temperature for 1 h and a mixture of 10 mL white fuming  $\text{HNO}_3$  (Sigma-Aldrich) and 20 mL concentrated  $\text{H}_2\text{SO}_4$  sonicating at 60 °C for 2 h, respectively. Both of the oxidized CNTs (oCNTs) were then centrifuged and washed with DI water and ethanol 3 times. The oxidized CNTs were noted as oCNTs ( $\text{KMnO}_4$ ) and oCNTs ( $\text{HNO}_3$ ), respectively. Except for these two categories of oCNTs with specific designation in the parenthesis, all other oCNTs appear in this work are oxidized by fuming nitric acid as mentioned in Section 2.2.

### 2.2. Catalyst preparation

To prepare the cobalt oxide ( $\text{Co}_3\text{O}_4$ ) supported on pre-oxidized CNTs, commercial CNTs doped with nitrogen were oxidized in white fuming  $\text{HNO}_3$  for an hour. The resulting oCNTs were dispersed in a mixture of ethanol and DI water in a ratio of 48:1 by volume (24 mL: 0.5 mL). 50 mg of cobalt acetate ( $\text{Co}(\text{C}_2\text{H}_3\text{O}_2)_2 \cdot 4\text{H}_2\text{O}$ , Sigma-Aldrich), 1.7 times that of the oCNTs, was dissolved by sonication for 20 min. Then 0.5 mL of 30 wt% ammonia (Sigma-Aldrich) was added into the solution to control the hydrolysis rate through complexation with the metal precursors. The reaction was carried out at 80 °C overnight. The purple supernatant was then removed by centrifuge. The precipitant was transferred into ethanol in a Teflon sealed Parr Bomb to allow hydrothermal treatment at 160 °C in a muffle furnace in air for 5 h and then washed with ethanol and DI water. The final step was annealing at 250 °C in 5%  $\text{NH}_3/\text{Ar}$  for 6 h and increase to 900 °C within 0.5 h to crystallize the particles and reduce the metal oxides as well as the remaining oxygen groups on the CNT surface.

To compare different oxidation agents listed in Section 2.1, metal oxides were grown on oCNTs ( $\text{KMnO}_4$ ) and oCNTs ( $\text{HNO}_3$ ) using the same procedure, only with a higher amount of metal precursor, 250 mg of cobalt acetate, respectively.

### 2.3. Physical characterization

The  $\text{Co}_3\text{O}_4$ /oCNT hybrid structure and structural variations between batches were evaluated using a Bruker D8 Advance X-ray diffractometer with a  $\text{Cu K}\alpha 1$  ceramic X-ray tube ( $\lambda = 0.1540562 \text{ nm}$ ) and a LynxEye Super Speed detector. The diffraction angle ( $2\theta$ ) was varied from 5° to 90° at a scanrate of 0.0285°/s. X-ray photoelectron spectroscopy (XPS) was performed using a Physical Electronics multiprobe with a Perkin-Elmer dual

anode X-ray source and a Kratos AXIS-165 surface analysis system to investigate the surface composition of the metal oxides and functional group distribution on the CNT surface. FTIR was collected with a Nicolet iS10 spectrophotometer with a wavenumber resolution of 4  $\text{cm}^{-1}$  to confirm the presence of various functional groups. The spectra were collected in attenuated total reflectance (ATR) mode with a single bounce ZnSe crystal over 16 scans. The morphology and metal oxide distribution along the CNTs were investigated by transmission electron microscopy (TEM) with a Tecnai T-12 and a FasTEM JEOL 2010 (high-resolution TEM).

### 2.4. Electrochemical characterization

Electrochemical experiments were carried out in a three-electrode electrochemical cell with a water jacket. A Pt wire and a double-junction  $\text{Hg}/\text{HgSO}_4$  electrode (Pine Research Instruments) were used as the counter and reference electrodes, respectively. Polarization curves for the ORR/OER were recorded using a VersaSTAT 3 potentiostat (Princeton Applied Research). The electrolyte used in the electrochemical tests was  $\text{O}_2$ -saturated 0.1 M potassium hydroxide (KOH) solution prepared from KOH crystals ( $\geq 85.0\%$  Sigma-Aldrich). All the polarization curves for activity comparisons and durability tests were collected with the scan rate of 5 mV/s and electrode rotation rate of 1600 rpm. The reference electrode was converted to (reversible hydrogen electrode) RHE by calibrating the  $\text{Hg}/\text{HgSO}_4$  electrode with hydrogen reference electrode (eDAQ, ET070 Hydroflex™ Hydrogen Reference Electrode) prior to every set of experiment. The working electrode was prepared by depositing the electrocatalyst ink onto a mirror-polished 5 mm-diameter glassy carbon electrode (GCE) (Pine Research Instrumentation). The GCE was polished to a mirror finish using a 0.05  $\mu\text{m}$  alumina-particle suspension (Buehler) on a moistened polishing microcloth (Buehler) and washed ultrasonically with ultra-pure 18.2 MΩ deionized water (from a Millipore Direct-Q 3UV purification system) for 4 min prior to each experiment. The catalyst ink dispersion (2 mg catalyst: 0.3 mL isopropanol: 0.7 mL DI water: 8  $\mu\text{L}$  5 wt% Nafion solution) was prepared by sonication for 20 min, forming a uniform suspension. 8  $\mu\text{L}$  of the suspension was added dropwise onto the GCE with a micropipet and then dried in air for 60 min on an inverted rotating disk electrode (RDE) at 300 RPM (Pine Research Instrumentation). A homogeneous black thin film was formed on top of the GCE. The loading of catalyst on the working electrode was approximately 16  $\mu\text{g}/\text{cm}^2$ .

## 3. Results and discussion

### 3.1. Oxidation agents

In order to grow transition metal oxides onto CNTs forming valence bond between oxides and supports to promote adhesion, the CNTs need to be functionalized initially to provide enough anchoring sites for metal oxides. One of the most common ways to introduce oxygen functional groups to carbon materials is chemical oxidation. The various oxygen functional groups introduced in this process may include the generally present carboxyls, carboxylic anhydrides, and lactones, as well as aldehydes, ethers, hydroxyl groups exhibiting phenolic character, carbonyl groups such as quinones or pyrones. [23–25] Datsyuk et al. measured the oxidation degree of multi-walled CNTs treated by different oxidation agents through Raman spectroscopy and X-ray photoelectron spectroscopy [26]. They concluded that the increase of surface oxidation degree follows the trend of hydrochloric acid < ammonium hydroxide/hydrogen peroxide < piranha < refluxed nitric acid. Treatment with all these oxidizing agents, except nitric acid, does not lead to production of additional defects on the outer walls of multi-walled

CNTs. Therefore, the oxidants used in this work were narrowed down to nitric acid and potassium permanganate [27]. The two batches of oCNTs used in our study were oxidized (KMnO<sub>4</sub> and HNO<sub>3</sub>) for different lengths of time to achieve the same overall oxidation degree.

The high-resolution C 1s XPS spectra of the oCNTs (KMnO<sub>4</sub>) (Fig. 1a) and oCNTs (HNO<sub>3</sub>) (Fig. 1b) were collected with pass energy of 50 eV within binding energy window from 280 eV to 294 eV, which was determined by the survey scan from 0 to 1100 eV with a 100 eV pass energy (Fig. S1a). Both high-resolution C 1s spectra of the oCNTs were analyzed with Gaussian fitting model and Linear curve as the background to control the full width at half maximum height of all the fitted peaks between 1.78–1.82. Then both C 1s spectra deconvoluted into 5 bands, corresponding to (from low to high binding energy): graphitic carbon at 284.5 eV, carbon singly bound to oxygen in phenols and ethers like C–O at 286.1 eV, carbon doubly bound to oxygen in ketones and quinones such as C=O at 287.5 eV, carbon bound to two oxygens in carboxyls, carboxylic anhydrides, and esters (i.e., –COO) at 288.7 eV, and the characteristic shakeup line of carbon in aromatic compounds at 290.5 eV ( $\pi$ – $\pi^*$  transition), respectively [28,29]. They demonstrated similar associated oxygen percentages, leaving the graphitic C percentage around 52%. But they presented different composition of the functionalized carbon. The oCNT (KMnO<sub>4</sub>) exhibited a larger shoulder in higher binding energy (around 289 eV) area showing higher percentage of carbon doubly bound to oxygen and bound to two oxygens. The deconvolution of the O 1s spectrum of oCNTs (KMnO<sub>4</sub>) (Fig. 1c) and oCNTs (HNO<sub>3</sub>) (Fig. 1d) results in two peaks: oxygen doubly bound to carbon (i.e., O=C) in quinones, ketones, and aldehydes at 531.6 eV, and oxygen singly bound to carbon (i.e., O–C) in ethers and phenols at 533.2 eV. But the difference between the two is that the ratio of C–O double bonds to single bonds is 1:1 for oCNTs (KMnO<sub>4</sub>), similar to literature value [30] and 1:2 for oCNTs (HNO<sub>3</sub>) [28], corresponding well with the C 1s analysis.

These variations in surface oxidation may account for the different crystallization status seen in TEM images (Fig. 2), which revealed differences in nucleation and distribution of the metal oxides along the oCNTs. The batch oxidized by KMnO<sub>4</sub> shown in Fig. 2a exhibited dendrite crystallization, forming islands among particles with much uncovered CNT surface area. However, the batch oxidized by HNO<sub>3</sub> shown in Fig. 2b obtained a single layer coverage with homogeneous particle distribution, indicating that with the similar defect sites on the CNT surface (maybe more on oCNTs prepared with KMnO<sub>4</sub> due to the more destructive structure of double bonds than single bonds with the same amount of oxygen associated to the surface), oxidizing by nitric acid may introduce more efficient anchoring sites for metal oxides, with less corrosion on CNT surface. This would be further elaborated on during discussion of the oxide-support bridging mechanism in Section 3.3.

### 3.2. X-ray diffraction (XRD)

XRD was used to understand the crystal structure and structural transformations of synthesized cobalt oxide catalysts before and after NH<sub>3</sub> treatment (Fig. 3). The five major characteristic peaks of the well-defined face-centered cubic Co<sub>3</sub>O<sub>4</sub> (red) appeared at 2 $\theta$  values of 31.27, 36.85, 44.81, 59.36 and 65.24°, which correspond to the (220), (311), (400), (511) and (440) reflections (JCPDS 43-1003, red triangles), respectively [19]. Two peaks appeared at 26.2° and 43.2°, indicated with black squares, corresponding to the (002) and (100) planes of the MWCNTs, respectively [31,32]. After NH<sub>3</sub> treatment (blue pattern), the Co<sub>3</sub>O<sub>4</sub> character decreased with the disappearance of the (511) and (440) peaks and a slight shift of the two major peaks at 36.85, 44.81° to lower 2 $\theta$  values, which are closer to the (101) and (110) facets of the CoO phase at 36.62 and 42.36° (JCPDS 65-5474, blue dots) [21]. However, it is unlikely

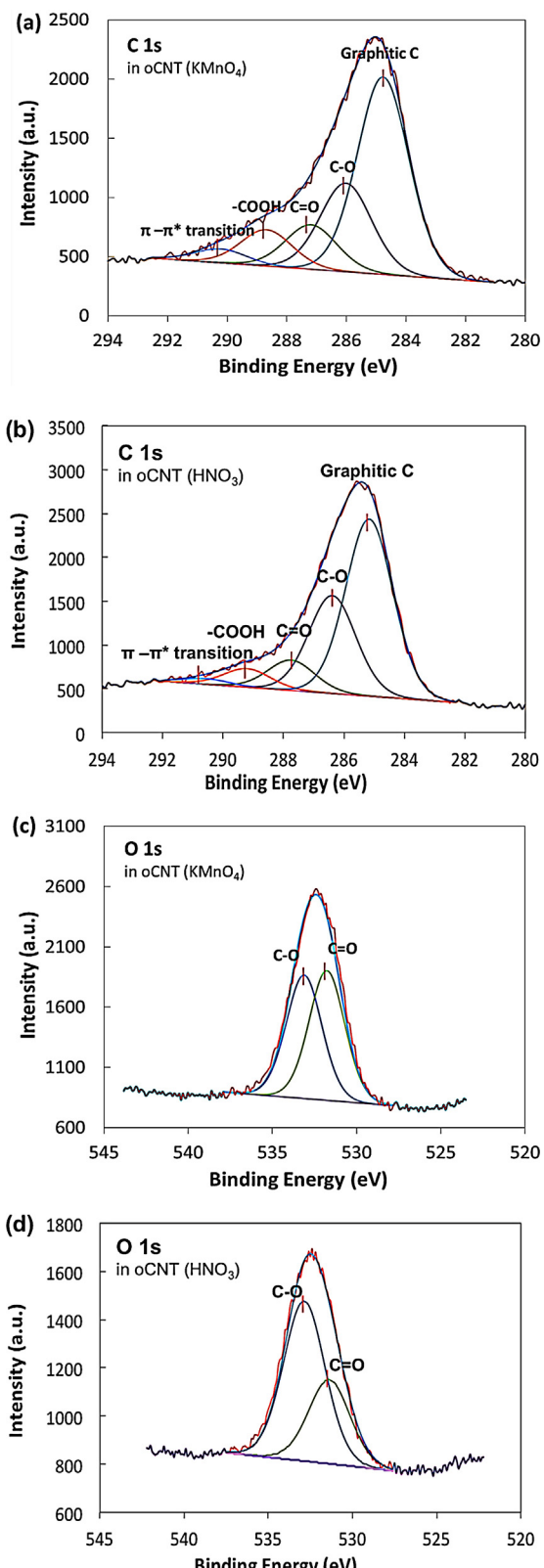


Fig. 1. XPS spectra of high resolution C 1s in (a) oCNTs (KMnO<sub>4</sub>); (b) oCNTs (HNO<sub>3</sub>); O 1s in (c) oCNTs (KMnO<sub>4</sub>); (d) oCNTs (HNO<sub>3</sub>).

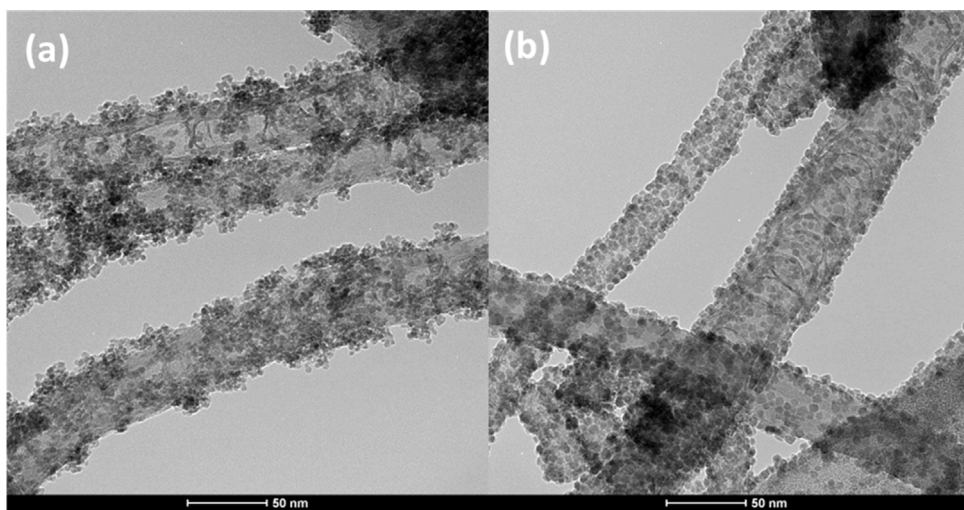


Fig. 2. TEM images of (a)  $\text{Co}_3\text{O}_4$ /oCNT( $\text{KMnO}_4$ ); (b)  $\text{Co}_3\text{O}_4$ /oCNT( $\text{HNO}_3$ ) with  $\text{Co}(\text{C}_2\text{H}_3\text{O}_2)_2 \cdot 4\text{H}_2\text{O}$  to oCNT weight ratio of 15:1.

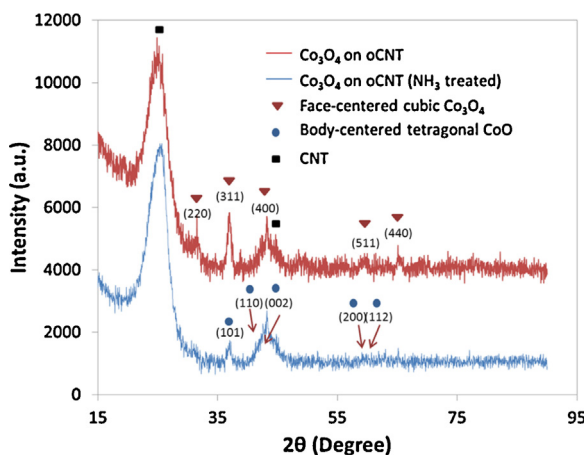


Fig. 3. XRD patterns of  $\text{Co}_3\text{O}_4$ /oCNT (red) and  $\text{NH}_3$  treated  $\text{Co}_3\text{O}_4$ /oCNT (blue). (For interpretation of the references to colour in this figure legend, the reader is referred to the web version of this article.)

that there was a complete phase transition to  $\text{CoO}$  because the two primary  $\text{CoO}$  peaks corresponding to the (200) and (112) reflections did not emerge. Therefore, the oxide is likely an amalgam of one  $\text{Co}$  (III) and two  $\text{Co}$  (II) states, which was explored by X-ray Photoelectron Spectroscopy.

### 3.3. X-ray photoelectron spectroscopy (XPS)

The C 1s high-resolution spectra for the as-oxidized CNTs,  $\text{Co}_3\text{O}_4$ /oCNT and  $\text{NH}_3$  treated  $\text{Co}_3\text{O}_4$ /oCNT samples are shown in Fig. 4a–c. The C spectrum in oxidized CNTs (Fig. 4a) was deconvoluted into 5 bands, corresponding to (from low to high binding energy): graphitic carbon (284.5 eV), carbon singly bound to oxygen (286.1 eV) in phenols and ethers like  $\text{C}-\text{O}$ , carbon doubly bound to oxygen (287.5 eV) in ketones and quinones, carbon bound to two oxygens (288.3 eV) in carboxyls, carboxylic anhydrides, and esters (i.e.,  $-\text{COO}$ ), and the  $\pi-\pi^*$  transition (290.1 eV), respectively. The surface C associated with O was about 46.3% and graphitic carbon was still the main component. After growing  $\text{Co}_3\text{O}_4$  along the oCNT surface, the percentage of C associated with O increased from 46.3% to 62.9% (Fig. 4b) and no additional C–metal bonds appeared suggesting that the anchoring bridges for the metal intermediates were oxygen functional groups. The increase of  $-\text{C}=\text{O}$  and  $-\text{COO}-$  (Table 1) during Co deposition may exclude the possibility

of growing metal oxides by breaking double bonds between C and O. One possible explanation is that single bond  $-\text{C}-\text{O}-$  provided the anchoring sites [18] by attracting the metal ions first, then the oxygen or hydroxide groups in the metal intermediate formed single bonds to neighboring C and some were further oxidized. This led to the significant increase of the portion of  $-\text{C}=\text{O}$  and  $-\text{C}=\text{O}$  bonds. After post-treatment with  $\text{NH}_3$ , the portion of both single and double bonds decreased significantly (Fig. 4c).

The deconvolution of the Co 2p spectrum in  $\text{Co}_3\text{O}_4$ /oCNT resulted in two doublets (Fig. S1b), with the two main peaks corresponding to Co 2p 3/2 in  $\text{Co}_3\text{O}_4$  at 779.95 eV and Co 2p 1/2 in  $\text{Co}_3\text{O}_4$  at 795.78 eV, respectively. The satellite doublets with binding energy ca. 6 eV higher than the major peaks are the characteristic satellites of  $\text{Co}^{2+}$  in  $\text{CoO}$ , since  $\text{Co}_3\text{O}_4$  is actually a mixture of  $\text{Co}$  (III) and  $\text{Co}$  (II) and the binding energy of the  $\text{Co}^{2+}$  in  $\text{CoO}$  and  $\text{Co}_3\text{O}_4$  are too close to separate. Therefore, the increase of the satellite doublets from 19.2% to 29.0% (Fig. S1c) suggest more reduced  $\text{CoO}$  in the catalyst, which agrees well with the XRD results.

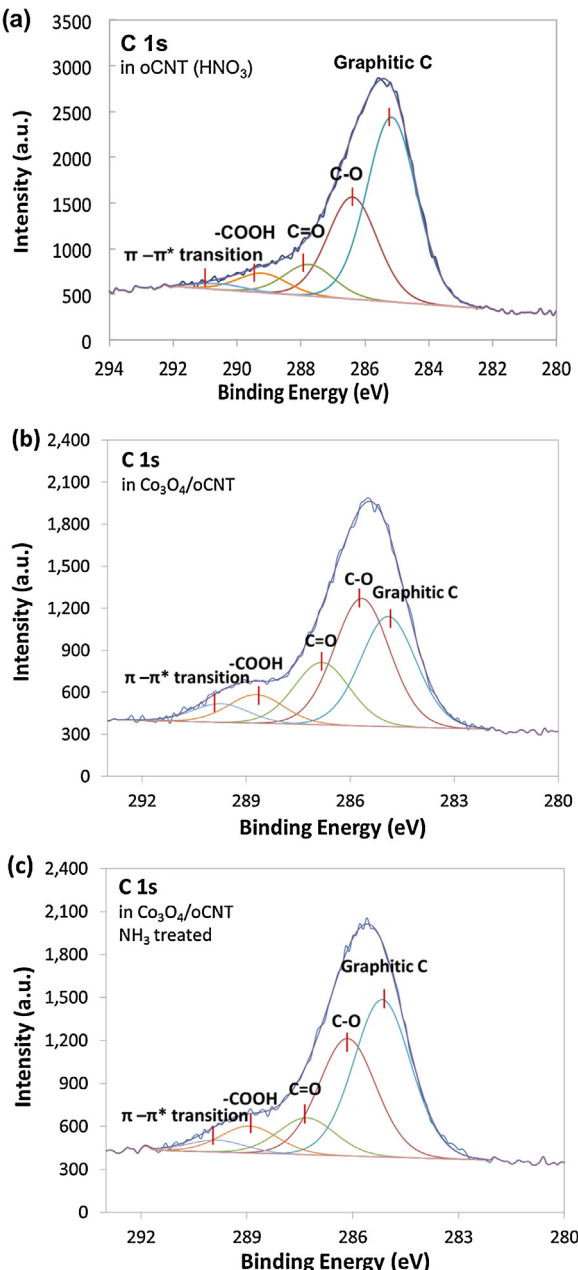
### 3.4. Fourier transform infrared spectroscopy (FTIR)

The FTIR spectra of the oxidized CNTs,  $\text{Co}_3\text{O}_4$ /oCNT and  $\text{NH}_3$  treated  $\text{Co}_3\text{O}_4$ /oCNT are shown in Fig. 5. The oxidized CNTs (purple) showed two absorption peaks at intermediate frequencies between  $1600\text{ cm}^{-1}$  and  $1100\text{ cm}^{-1}$ , which belong to  $\text{C}=\text{O}$ ,  $\text{C}=\text{C}$  and  $\text{C}=\text{N}$  bending from 1500 to  $2000\text{ cm}^{-1}$ , and  $\text{C}-\text{O}$ ,  $\text{C}-\text{C}$  and  $\text{C}-\text{N}$  bending from 1000 to  $1500\text{ cm}^{-1}$ , respectively [33–35]. This indicated the introduction of oxygen functional groups onto the CNTs after being oxidized with concentrated  $\text{HNO}_3$ . The peaks between  $1600\text{ cm}^{-1}$  and  $1100\text{ cm}^{-1}$  became more profound when cobalt oxides were introduced to the CNTs (blue and green), which may be due to the bond formation between the oxygen or hydroxide groups in the cobalt intermediate and the non-functionalized graphitic C after the metal ions were attracted by the anchoring oxygen bridges. Vibrations corresponding to the metal oxide were observed by the appearance of the absorption peaks at wavenumber below  $800\text{ cm}^{-1}$ . After  $\text{NH}_3$  treatment, the single and double bonds between oxygen and carbon decreased significantly (orange), similar to the as-oxidized CNTs. The peak representing metal oxides below  $800\text{ cm}^{-1}$  remained in the spectrum. The oxygen functional group increase and decrease trends after depositing  $\text{Co}_3\text{O}_4$  onto oCNTs and the ammonia reduction step matched well with the XPS results.

**Table 1**

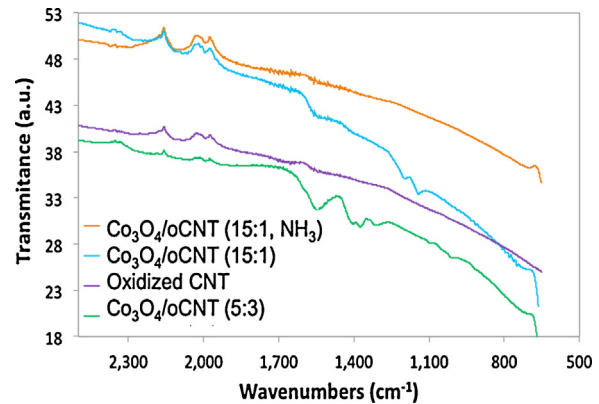
Relative Content of Functional Groups Determined by C 1s High-Resolution XPS Spectra.

Samples	Relative atomic concentrations (%)	Graphitic C		
		—C—O—	—C=O	—COO—
as-oxidized CNT	54.7	30.2	9.35	5.7
Co <sub>3</sub> O <sub>4</sub> /oCNT	33.5	38.8	19.0	8.7
NH <sub>3</sub> treated Co <sub>3</sub> O <sub>4</sub> /oCNT	45.1	37.3	10.9	6.7

**Fig. 4.** XPS spectra of high resolution C 1s in (a) oCNT; (b) Co<sub>3</sub>O<sub>4</sub>/oCNT; (c) NH<sub>3</sub> treated Co<sub>3</sub>O<sub>4</sub>/oCNT.

### 3.5. Transmission electron microscopy (TEM)

Fig. 6a and b show the morphology of Co<sub>3</sub>O<sub>4</sub>/oCNT with optimized cobalt precursor to oCNT weight ratio of 5:3, before and after ammonia treatment, respectively. Smaller particles with irregular oxide grains (ca. 1–4 nm in diameter) aggregated at specific areas along the tubes with much exposed oCNT surface before ammonia treatment. After treating the catalysts with NH<sub>3</sub> at low temperature

**Fig. 5.** FTIR spectra of oxidized CNT (purple); Co<sub>3</sub>O<sub>4</sub>/oCNT (Co(C<sub>2</sub>H<sub>3</sub>O<sub>2</sub>)<sub>2</sub>·4H<sub>2</sub>O:oCNT = 15:1) (green); Co<sub>3</sub>O<sub>4</sub>/oCNT (Co(C<sub>2</sub>H<sub>3</sub>O<sub>2</sub>)<sub>2</sub>·4H<sub>2</sub>O:oCNT = 5:3) (blue); NH<sub>3</sub> treated Co<sub>3</sub>O<sub>4</sub>/oCNT (Co(C<sub>2</sub>H<sub>3</sub>O<sub>2</sub>)<sub>2</sub>·4H<sub>2</sub>O:oCNT = 5:3) (orange). (For interpretation of the references to colour in this figure legend, the reader is referred to the web version of this article.)

(Fig. 6b), bundles of small particles grew larger (between 20 and 50 nm) with blunt edges, and much cleaner CNTs were achieved afterwards. High resolution TEM (HRTEM) in Fig. 6c clearly confirmed the hybrid structure of a single Co<sub>3</sub>O<sub>4</sub> particle supported on CNT from the ammonia treated sample in Fig. 6b. Part of the Co<sub>3</sub>O<sub>4</sub> particle was imbedded into the CNT even after heat treatment and a strong sonication, suggesting a strong interaction between CNT and Co<sub>3</sub>O<sub>4</sub> particles. Samples synthesized with different cobalt precursor to oCNT weight ratios and based on different oxidation degree of oCNTs were also compared in Figs. S2. A higher ratio (15:1) resulted in Co<sub>3</sub>O<sub>4</sub> grains being fully packed along the oCNTs without exposing any bare oCNT surface area (Fig. S2a). The larger single particles were cubic with side lengths of less than 10 nm. However, if only the degree of CNT oxidation was lowered (0.5 h with concentrated HNO<sub>3</sub>), as shown in Fig. S2d, the morphology of the single particles were hardly changed compared with Fig. S2a, and particle distribution was more sparse along the CNTs.

### 3.6. Electrochemical characterization

The ORR/OER activities of Co<sub>3</sub>O<sub>4</sub>/oCNT samples with the various synthesis parameters discussed in Section 3.4 and 3.5 are compared in Fig. S2. The sample presenting the best combination of activity and durability (discussed below) possessed the morphology and distribution shown in Fig. 6b (with fuming HNO<sub>3</sub> oxidizing for 1 h, metal precursor to oCNT weight ratio of 5:3 and additional ammonia reduction step). The ORR polarization curve of this top-performing Co<sub>3</sub>O<sub>4</sub>/oCNT was compared with commercial 50 wt% Pt/C (TEC10E50E, Tanaka) (Fig. 7a), with the same total catalyst loading, in O<sub>2</sub>-saturated 0.1 M KOH electrolyte. Both the ORR onset and half-wave potential of NH<sub>3</sub> treated Co<sub>3</sub>O<sub>4</sub>/oCNT were only about 0.1 V negative of commercial Pt/C. In addition, the OER onset potential, 1.48 V, was only 0.05 V higher than that of commercial iridium black (Fig. 7b), equaling the best-known Co<sub>3</sub>O<sub>4</sub>-based hybrid OER catalysts [21]. The ORR/OER activities were much improved over the starting N-CNT material shown in Fig. 7c. The excellent bifunctional activity demonstrated by the

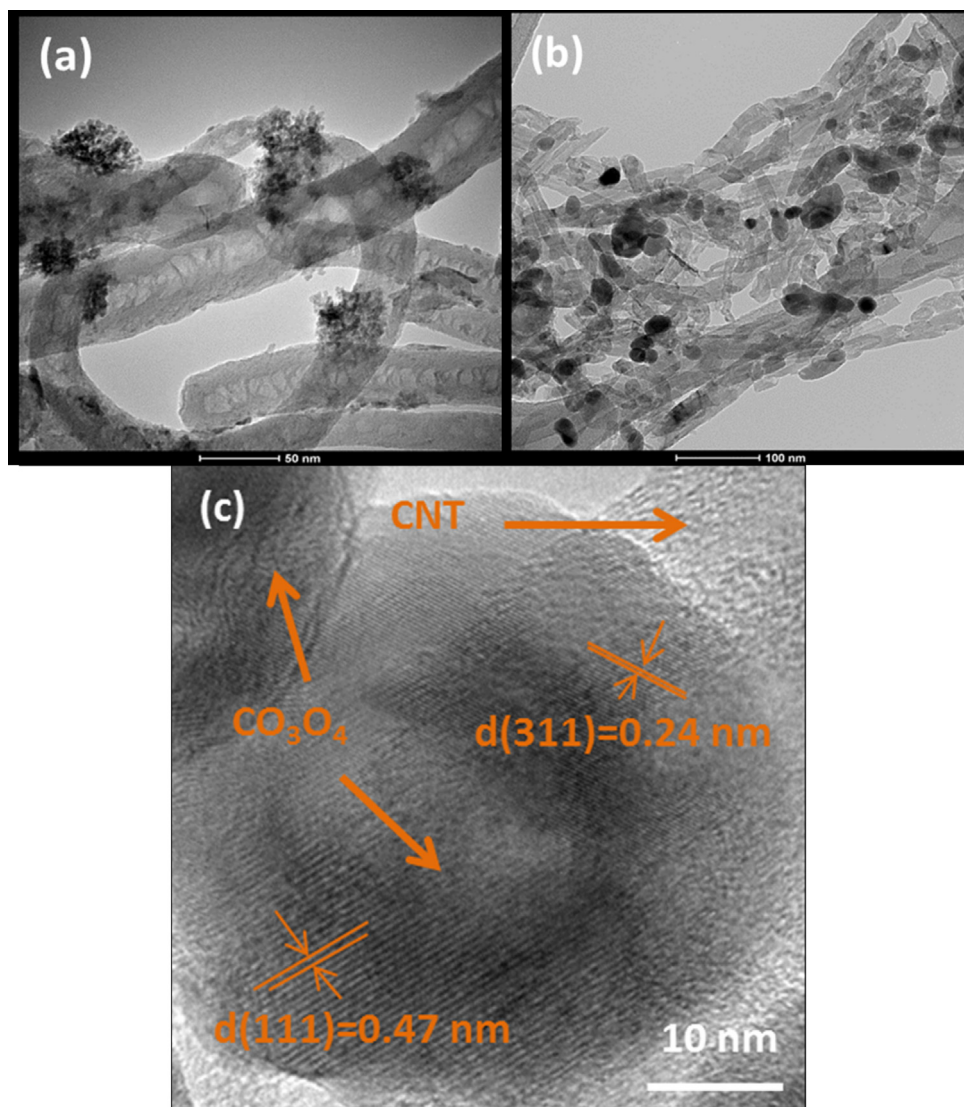


**Fig. 6.** TEM images of  $\text{Co}_3\text{O}_4/\text{oCNT}$  (a) before ammonia treatment; (b) after ammonia treatment (with  $\text{Co}(\text{C}_2\text{H}_3\text{O}_2)_2 \cdot 4\text{H}_2\text{O}$  to oCNT weight ratio of 5:3 for both (a) and (b)); (c) high-resolution TEM of Image 6b.

$\text{Co}_3\text{O}_4/\text{oCNT}$  catalyst is among the highest when compared to the literature [17,19,21].

Koutecky-Levich plots from the ORR polarization curves at different electrode rotation rates for both  $\text{NH}_3$  treated  $\text{Co}_3\text{O}_4/\text{oCNT}$  and commercial Pt/C are shown in Figs. 7 d and S3c, respectively. From 0.5 V to 0.75 V, linear Koutecky-Levich plots of  $\text{NH}_3$  treated  $\text{Co}_3\text{O}_4/\text{oCNT}$  (Fig. S3a) and Pt/C black (Fig. S3b) were obtained (assuming first order kinetics), by plotting  $J^{-1}$  vs.  $\omega^{-1/2}$  [36]. From Eqs. (1) and (2), the slopes ( $1/B$ ) of the Koutecky-Levich plots at different potentials yield the average number of electrons transferred,  $n$ , involved in the ORR in alkaline media.

$$1/J = 1/J_k + 1/J_{diff} = 1/J_k + 1/(B\omega^{1/2}) \quad (1)$$

$$B = 0.62nFC_0D_0^{2/3}\eta^{-1/6} \quad (2)$$

where  $J_k$  and  $J_{diff}$  are the kinetic and diffusion limited current densities respectively,  $F$  is the Faraday constant,  $C_0$  is the saturated concentration of  $\text{O}_2$  in the 0.1 M KOH electrolyte ( $1.21 \times 10^{-3}$  mol/L),  $D_0$  is the diffusion coefficient of  $\text{O}_2$  in the KOH electrolyte ( $1.86 \times 10^{-5}$  cm $^2$  s), and  $\eta$  is the viscosity of the electrolyte ( $1.008 \times 10^{-2}$  cm $^2$  s) [36]. Over the entire potential range,

it was found that for  $\text{NH}_3$  treated  $\text{Co}_3\text{O}_4/\text{oCNT}$ ,  $n \approx 4$  (on average) and for Pt/C,  $n \approx 3.6$ , close to reported literature values [37–39]. The lower electron transfer number of Pt/C could be linked to its higher degree of 2-electron ORR in alkaline media to produce peroxide-like intermediates when compared with  $\text{NH}_3$  treated  $\text{Co}_3\text{O}_4/\text{oCNT}$ .

Catalyst durability tests were first conducted on raw and oxidized CNTs (Fig. S4a and b). The ORR activity was significantly compromised after only 500 cycles at scan rate of 500 mV/s in  $\text{O}_2$ -saturated 0.1 M KOH electrolyte, which showed that the ammonia reduction step was necessary to restore structural and chemical stability to the CNTs. The stability of  $\text{NH}_3$  treated  $\text{Co}_3\text{O}_4/\text{oCNT}$  was investigated over 2000 cycles, from 0 to 1.9 V, at scan rate of 500 mV/s. The intermediate polarization curves were collected at 1600 rpm, 20 mV/s (Fig. 7e), demonstrating no significant change for both activities even after 2000 cycles in this harsh oxidizing environment. A new redox couple appeared during cycling (Fig. 7f), which verified the existence of cobalt oxide [40]. However, for the catalysts without any post  $\text{NH}_3$  treatment, the ORR activity was nearly absent within the first 50 cycles (Fig. S4c). Therefore, the  $\text{NH}_3$  reduction plays a critical role in the stabilization of the surface metal oxide and improvement of the CNT support's durability.

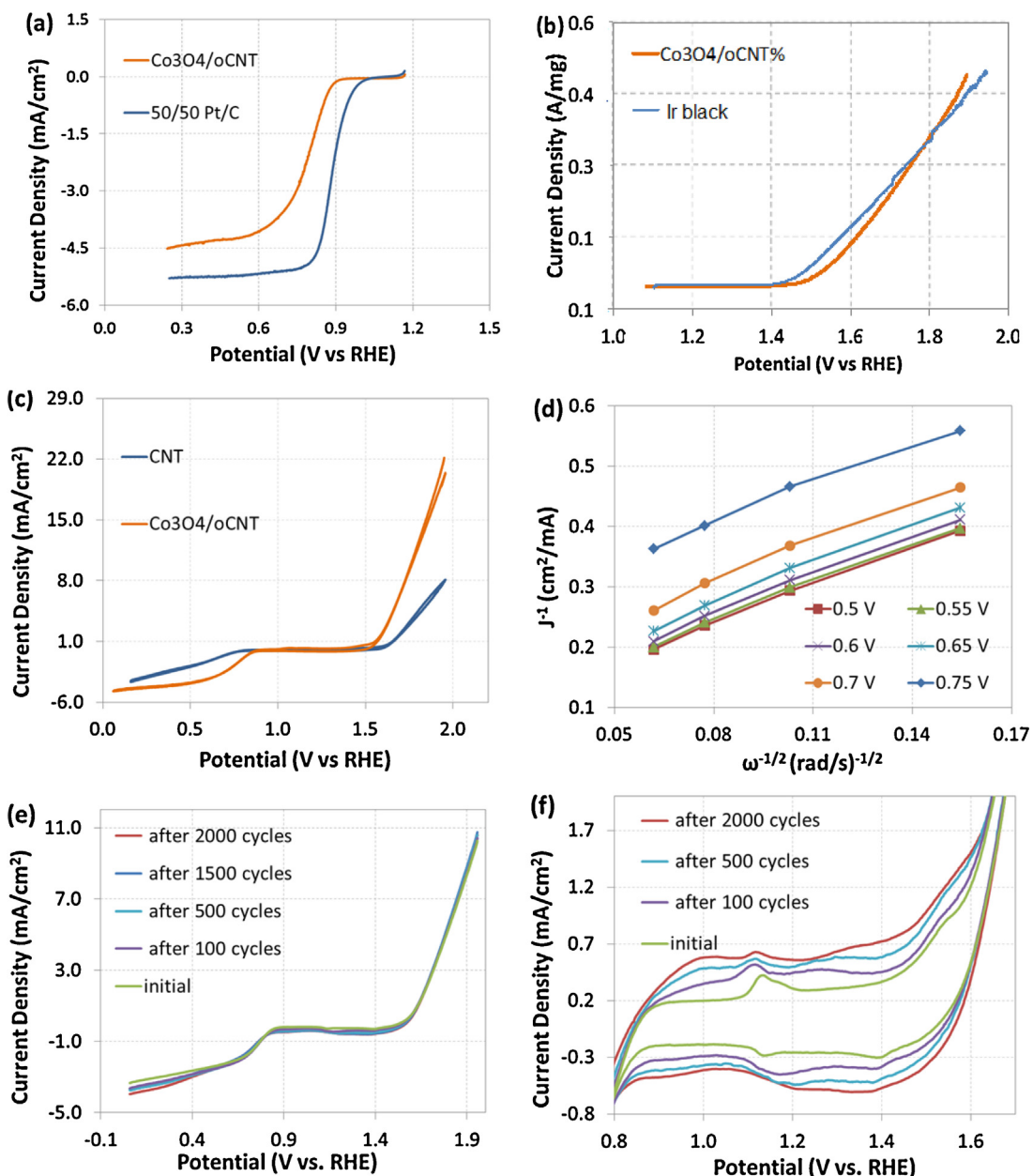


**Fig. 7.** (a) ORR polarization curve of NH<sub>3</sub> treated Co<sub>3</sub>O<sub>4</sub>/oCNT compared with that of commercial Pt/C; (b) OER polarization curve of NH<sub>3</sub> treated Co<sub>3</sub>O<sub>4</sub>/oCNT compared with that of commercial Ir black; (c) OER/ORR polarization curve of NH<sub>3</sub> treated Co<sub>3</sub>O<sub>4</sub>/oCNT compared with that of commercial raw N-CNT; (d) Koutecky-Levich plots of NH<sub>3</sub> treated Co<sub>3</sub>O<sub>4</sub>/oCNT from 0.5 V to 0.75 V; (e) durability test of NH<sub>3</sub> treated Co<sub>3</sub>O<sub>4</sub>/oCNT for 2000 cycles; (f) zoom-in plot from 0.8 to 1.6 V of Fig. 7e. (For interpretation of the references to colour in this figure legend, the reader is referred to the web version of this article.)

#### 4. Conclusion

A highly stable, ORR/OER active, bifunctional, CNT-based hybrid catalyst for reversible alkaline fuel cells was obtained at the bench scale. For the first time, a carbon based hybrid material demonstrated significant durability over a large potential range from 0.0V to 1.9V for 2000 cycles. This study examined the impact of the synthesis approach, oxidation agent, metal oxide anchoring bridges, particle morphology, and metal oxidation states to functional groups reduction, in order to provide an optimization pathway and new insights for next generation catalyst design. Future work will focus on optimizing parameters in the procedure, such as oxidizing conditions, precursor substitution, CNT size, post-

treatment, etc. Eventually, the novel materials will be scaled up to test in unitized regenerative fuel cells.

#### Acknowledgement

The project is financially supported by the Department of Energy's Fuel Cell Technology Office under the Grant DE-EE0006960.

#### Appendix A. Supplementary data

Supplementary data associated with this article can be found, in the online version, at <http://dx.doi.org/10.1016/j.apcatb.2016.09.048>.

## References

[1] B. Pivovar, F.C.T. Leader, P. Fedkiw, A.R.O.R. Mantz, A.R.O.B. Pivovar, T. Zawodzinski, et al., Alkaline membrane fuel cell workshop final report, in: Work. Held December, 2006: p. 13.

[2] J.R. Varcoe, P. Atanassov, D.R. Dekel, A.M. Herring, M.A. Hickner, P.A. Kohl, et al., Anion-exchange membranes in electrochemical energy systems, *Energy Environ. Sci.* 7 (2014) 3135–3191.

[3] H. Zhu, S. Zhang, Y. Huang, L. Wu, S. Sun, Monodisperse  $M_xFe_{3-x}O_4$  ( $M = Fe, Cu, Co, Mn$ ) nanoparticles and their electrocatalysis for oxygen reduction reaction, *Nano Lett.* 13 (2013) 2947–2951.

[4] P. Manivasakan, P. Ramasamy, J. Kim, Use of urchin-like  $Ni_xCo_{3-x}O_4$  hierarchical nanostructures based on non-precious metals as bifunctional electrocatalysts for anion-exchange membrane alkaline alcohol fuel cells, *Nanoscale* 6 (2014) 9665–9672.

[5] T. Maiyalagan, K.a. Jarvis, S. Therese, P.J. Ferreira, A. Manthiram, Spinel-type lithium cobalt oxide as a bifunctional electrocatalyst for the oxygen evolution and oxygen reduction reactions, *Nat. Commun.* 5 (2014) 3949.

[6] Y.J. Sa, K. Kwon, J.Y. Cheon, F. Kleitz, S.H. Joo, Ordered mesoporous  $Co_3O_4$  spinels as stable, bifunctional, noble metal-free oxygen electrocatalysts, *J. Mater. Chem. A* 1 (2013) 9992.

[7] Y. Meng, W. Song, H. Huang, Z. Ren, S.Y. Chen, S.L. Suib, Structure-property relationship of bifunctional  $MnO_2$  nanostructures: highly efficient, ultra-stable electrochemical water oxidation and oxygen reduction reaction catalysts identified in alkaline media, *J. Am. Chem. Soc.* 136 (2014) 11452–11464.

[8] M. Fayette, a. Nelson, R.D. Robinson, Electrophoretic deposition improves catalytic performance of  $Co_3O_4$  nanoparticles for oxygen reduction/oxygen evolution reactions, *J. Mater. Chem. A* 3 (2015) 4274–4283.

[9] W. Tang, Y. Hou, F. Wang, L. Liu, Y. Wu, K. Zhu,  $LiMn_2O_4$  nanotube as cathode material of second-level charge capability for aqueous rechargeable batteries, *Nano Lett.* 13 (2013) 2036–2040.

[10] M. Gong, Y. Li, H. Wang, Y. Liang, J.Z. Wu, J. Zhou, et al., An advanced Ni-Fe layered double hydroxide electrocatalyst for water oxidation, *J. Am. Chem. Soc.* 135 (2013) 8452–8455.

[11] P. Li, Y. Yang, E. Shi, Q. Shen, Y. Shang, S. Wu, et al., Core-double-shell, carbon nanotube/polypyrrole/ $MnO_2$  sponge as freestanding, compressible supercapacitor electrode, *ACS Appl. Mater. Interfaces* 6 (2014) 5228–5234.

[12] R.-R. Bi, X.-L. Wu, F.-F. Cao, L.-Y. Jiang, Y.-G. Guo, L.-J. Wan, Highly dispersed  $RuO_2$  nanoparticles on carbon nanotubes: facile synthesis and enhanced supercapacitance performance, *J. Phys. Chem. C* 114 (2010) 2448–2451.

[13] Z. Chen, A. Yu, D. Higgins, H. Li, H. Wang, Z. Chen, Highly active and durable core – corona structured bifunctional catalyst for rechargeable metal – air battery application, *Nano Lett.* 12 (2012) 1946–1952.

[14] R. Ning, J. Tian, A.M. Asiri, A.H. Qusti, A.O. Al-Youbi, X. Sun, Spinel  $CuCo_2O_4$  nanoparticles supported on n-doped reduced graphene oxide: a highly active and stable hybrid electrocatalyst for the oxygen reduction reaction, *Langmuir* 29 (2013) 13146–13151.

[15] Q. Liu, J. Jin, J. Zhang,  $NiCo_2S_4$ /graphene as a bifunctional electrocatalyst for oxygen reduction and evolution reactions, *ACS Appl. Mater. Interfaces* 5 (2013) 5002–5008.

[16] Y. Hou, Z. Wen, S. Cui, S. Ci, S. Mao, J. Chen, An advanced nitrogen-doped graphene/cobalt-embedded porous carbon polyhedron hybrid for efficient catalysis of oxygen reduction and water splitting, *Adv. Funct. Mater.* 25 (2015) 872–882.

[17] G. Zhang, B.Y. Xia, X. Wang, X.W. David Lou, Strongly coupled  $NiCo_2O_4$ -rGO hybrid nanosheets as a methanol-tolerant electrocatalyst for the oxygen reduction reaction, *Adv. Mater.* 26 (2014) 2408–2412.

[18] G. Zhou, D.W. Wang, L.C. Yin, N. Li, F. Li, H.M. Cheng, Oxygen bridges between nio nanosheets and graphene for improvement of lithium storage, *ACS Nano* 6 (2012) 3214–3223.

[19] Y. Liang, Y. Li, H. Wang, J. Zhou, J. Wang, T. Regier, et al.,  $Co_3O_4$  nanocrystals on graphene as a synergistic catalyst for oxygen reduction reaction, *Nat. Mater.* 10 (2011) 780–786.

[20] Y. Liang, H. Wang, J. Zhou, Y. Li, J. Wang, T. Regier, et al., Covalent hybrid of spinel manganese-cobalt oxide and graphene as advanced oxygen reduction electrocatalysts, *J. Am. Chem. Soc.* 134 (2012) 3517–3523.

[21] S.K. Singh, V.M. Dhavale, S. Kurungot, Low surface energy plane exposed  $Co_3O_4$  nanocubes supported on nitrogen-doped graphene as an electrocatalyst for efficient water oxidation, *ACS Appl. Mater. Interfaces* 7 (2015) 442–451.

[22] S. Mao, Z. Wen, T. Huang, Y. Hou, J. Chen, High-performance bi-functional electrocatalysts of 3D crumpled graphene-cobalt oxide nanohybrids for oxygen reduction and evolution reactions, *Energy Environ. Sci.* 7 (2014) 609–616.

[23] M.L. Toebes, J.M.P. van Heeswijk, J.H. Bitter, A.J. Van Dillen, K.P. de Jong, The influence of oxidation on the texture and the number of oxygen-containing surface groups of carbon nanofibers, *Carbon N. Y.* 42 (2004) 307–315.

[24] T.G. Ros, A.J. Van Dillen, J.W. Geus, D.C. Koningsberger, Surface oxidation of carbon nanofibres, *Chem. Eur. J.* 8 (2002) 1151–1162.

[25] M.T. Martí, M.A. Callejas, A.M. Benito, M. Cochet, T. Seeger, A. Anson, et al., Sensitivity of single wall carbon nanotubes to oxidative processing: structural modification, intercalation and functionalisation, *Carbon N. Y.* 41 (2003) 2247–2256.

[26] V. Datsyuk, M. Kalyva, K. Papagelis, J. Parthenios, D. Tasis, A. Siokou, et al., Chemical oxidation of multiwalled carbon nanotubes, *Carbon N. Y.* 46 (2008) 833–840.

[27] W.S. Hummers Jr., R.E. Offeman, Preparation of graphitic oxide, *J. Am. Chem. Soc.* 80 (1958) 1339.

[28] Y. Xing, L. Li, C.C. Chusuei, R.V. Hull, Sonochemical oxidation of multiwalled carbon nanotubes, *Langmuir* 21 (2005) 4185–4190.

[29] S. Kundu, Y. Wang, W. Xia, M. Muhler, Thermal stability and reducibility of oxygen-containing functional groups on multiwalled carbon nanotube surfaces: a quantitative high-resolution xps and TPD/TPR study, *J. Phys. Chem. C* 112 (2008) 16869–16878.

[30] D.V. Kosynkin, A.L. Higginbotham, A. Sinitskii, J.R. Lomeda, A. Dimiev, B.K. Price, et al., Longitudinal unzipping of carbon nanotubes to form graphene nanoribbons, *Nature* 458 (2009) 872–876.

[31] L. Zhu, W. Wu, Y. Zhu, W. Tang, Y. Wu, Composite of  $CoOOH$  nanoplates with multiwalled carbon nanotubes as superior cathode material for supercapacitors, *J. Phys. Chem. C* 119 (2015) 7069–7075.

[32] M. Xu, D.N. Futaba, M. Yumura, K. Hata, Tailoring temperature invariant viscoelasticity of carbon nanotube material, *Nano Lett.* 11 (2011) 3279–3284.

[33] L. Shahriary, A.a. Athawale, Graphene oxide synthesized by using modified hummers approach, *Int. J. Renew. Energy Environ. Eng.* 02 (2014) 58–63.

[34] C.-T.C. Jianguo Song, Xinzhai Wang, Preparation and characterization of graphene oxide, *J. Nanomater.* (2014), 2014.

[35] B.H. Stuart, Spectral analysis, in: *Infrared Spectrosc. Fundam. Appl.*, John Wiley & Sons, Ltd, 2005, pp. 45–70.

[36] N.A. Anastasijević, V. Vesović, R.R. Adžić, Determination of the kinetic parameters of the oxygen reduction reaction using the rotating ring-disk electrode: part I. Theory, *J. Electroanal. Chem. Interfacial Electrochem.* 229 (1987) 305–316.

[37] L. Genies, R. Faure, R. Durand, Electrochemical reduction of oxygen on platinum nanoparticles in alkaline media, *Electrochim. Acta* 44 (1998) 1317–1327.

[38] N. Ramaswamy, S. Mukerjee, Fundamental mechanistic understanding of electrocatalysis of oxygen reduction on Pt and non-Pt surfaces: acid versus alkaline media, *Adv. Phys. Chem.* 2012 (2012).

[39] S. Zhao, A.E. Wangstrom, Y. Liu, W.A. Rigdon, W.E. Mustain, Stability and activity of Pt/ITO electrocatalyst for oxygen reduction reaction in alkaline media, *Electrochim. Acta* 157 (2015) 175–182.

[40] M.S. Burke, M.G. Kast, L. Trotochaud, A.M. Smith, S.W. Boettcher, Cobalt–iron (oxy) hydroxide oxygen evolution electrocatalysts: the role of structure and composition on activity, stability, and mechanism, *J. Am. Chem. Soc.* 137 (2015) 3638–3648.